Supplementary Information for:

Pioneering non-thermal plasma as a defect passivator: a new Frontier in ambient metal halide perovskite synthesis

Milad Mahiny[a,b,*], Hossein Lotfi[b], Maryam Beigmohammadi[c], Mehdi Pooriraj[d], Maryam Heydari[a,e], Alireza Shirzad[a,e], Hamidreza Mahfouzi[f], Mohammad Khaja Nazeeruddin[g,*], Abd. Rashid bin Mohd Yusoff[h,*], Hossein Movla[a,e,*]

[a]*Faculty of Physics University of Tabriz 51666-14766 Tabriz Iran*
[b]*Research Institute for Applied Physics and Astronomy University of Tabriz 51666-14766 Tabriz Iran*
[c]*Department of Optical & Laser Engineering University of Bonab 55517-61167 Bonab Iran*
[d]*Department of Semiconductors Materials and Energy Research Center (MERC) 31787-316 Tehran Iran*
[e]*Western Plasma Technologies Inc. 2727 28 Ave SE Calgary T2B0L4 Alberta Canada*
[f]*Department of Biomechanics Faculty of Biomechanics Engineering Sahand University of Technology 51335-1996 Tabriz Iran*
[g]*Institute of Chemical Sciences and Engineering Ecole Polytechnique Federale de Lausanne (EPFL) Sion Switzerland*
[h]*Department of Physics Faculty of Science Universiti Teknologi Malaysia Johor Bahru Malaysia*

[*]Corresponding authors:
Hossein Movla (h.movla@westernplasma.com)
Abd. Rashid bin Mohd Yusoff (abdrashid.my@utm.my)
Mohammad Khaja Nazeeruddin (mdkhaja.nazeeruddin@epfl.ch)
Milad Mahiny (miladmhi.97@ms.tabrizu.ac.ir)

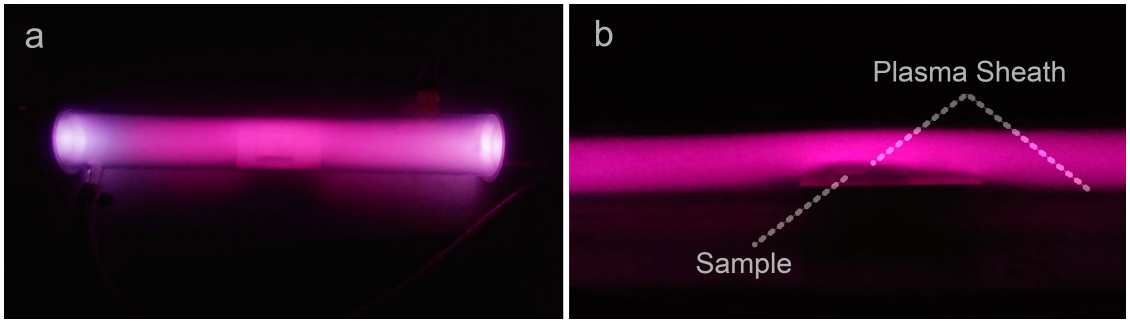

Fig. S1 Glow discharge plasma: (a) side view of the plasma reactor, (b) end view displaying the uniform pink non-thermal plasma and the visible plasma sheath. The glow discharge was achieved using nitrogen (N_2) gas, providing a highly reactive environment conducive to the formation of perovskite materials.

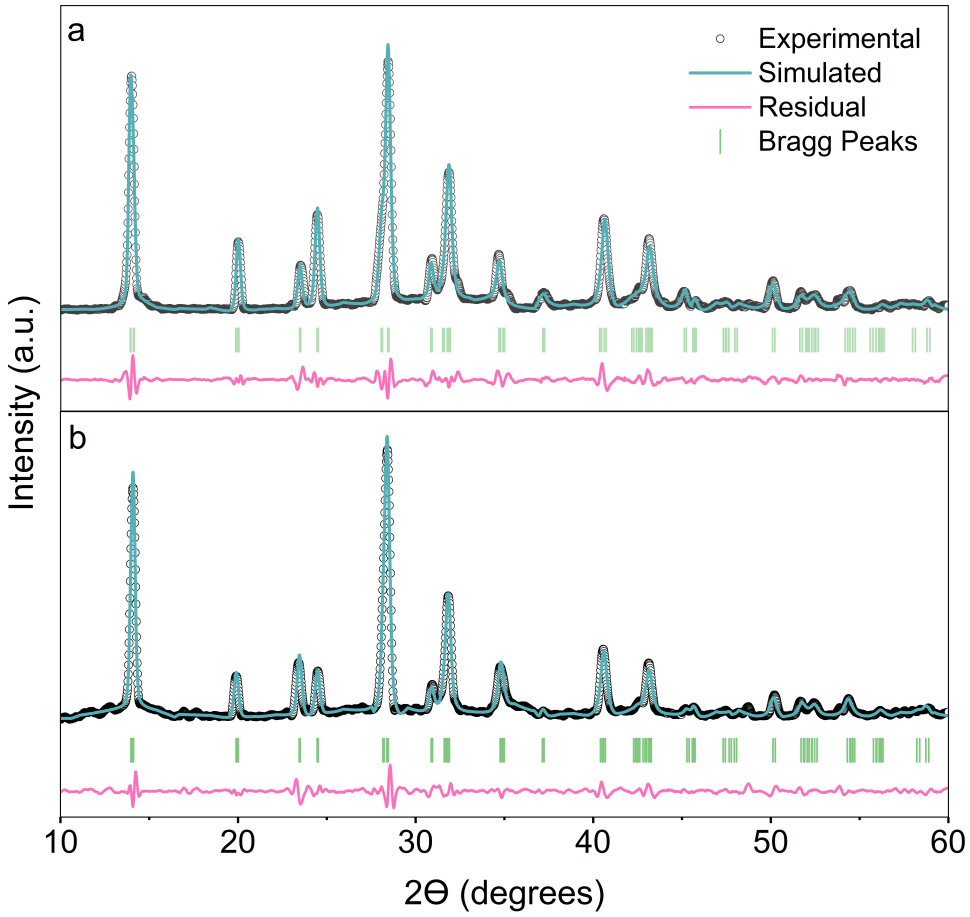

Fig. S2 Rietveld refinement analysis of the XRD patterns of (a) AC and (b) DC non-thermal plasma synthesis. The XRD patterns showcase distinct peaks that are sharp and well-resolved, indicative of the tetragonal phase with the $I4/cm$ space group.

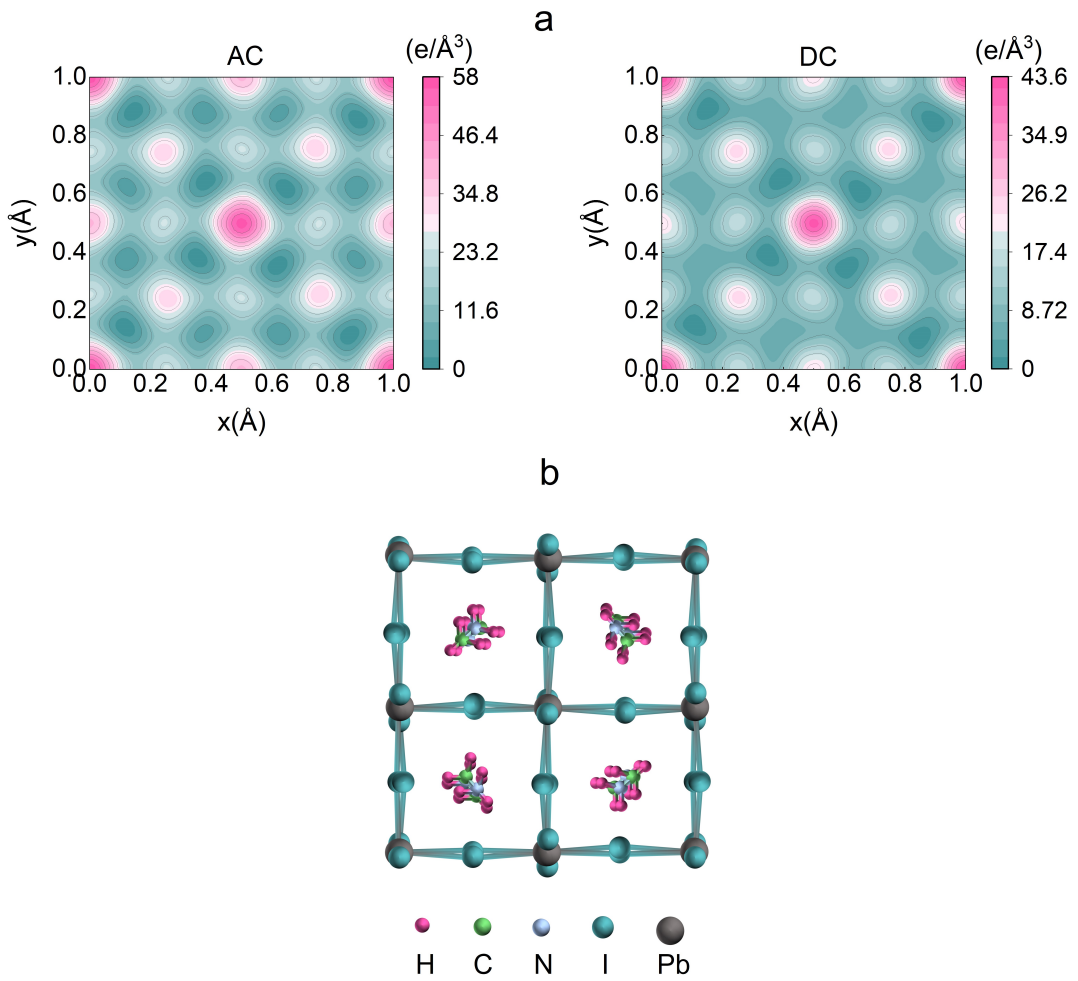

Fig. S3 Rietveld-refined XRD analysis of $MAPbI_3$: (a) electron density and (b) molecular structure. AC-NTP treated samples show pronounced maxima at Pb and I sites, indicating strong ionic bonds and a well-ordered lattice, while DC plasma-treated samples exhibit less distinct peaks, suggesting a more disordered lattice and potential intrinsic point defects.

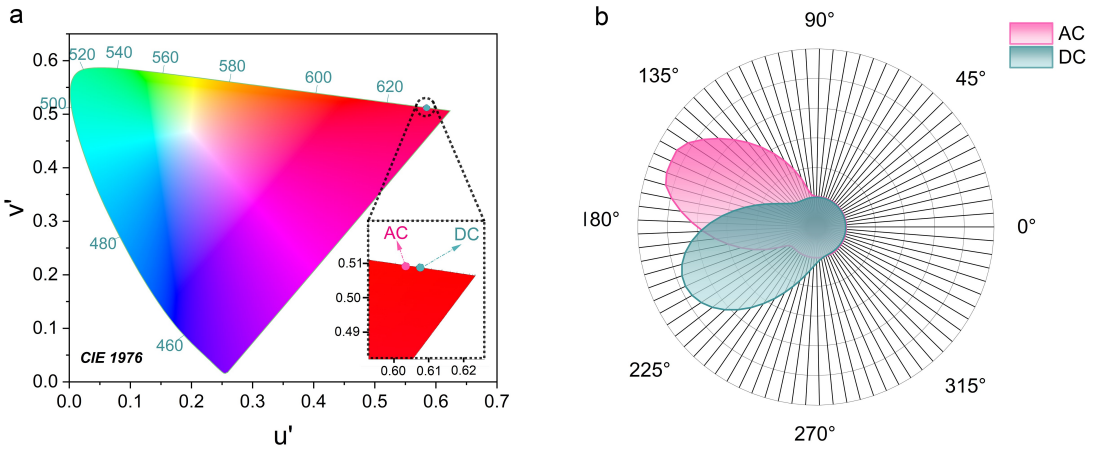

Fig. S4 (a) CIE 1976 chromaticity diagram showing the color coordinates of $CH_3NH_3PbI_3$ synthesized using AC and DC non-thermal plasma, (b) polar plot illustrating the angular distribution of PL emission from the synthesized perovskite, comparing the effects of AC (rose) and DC (teal) plasma processes.

Supplementary Note S1:

The DFT study presented showcases advanced first principles calculations to investigate the electronic structure of $MAPbI_3$ perovskite, a material of significant interest for its photovoltaic properties. Utilizing Quantum Espresso, the study meticulously differentiates between the cubic ($Pm3m$) and the more complex tetragonal ($I4/cm$) phases.

Fig. S5a and d illustrate the electron density maps for the tetragonal and cubic phases, respectively. In the tetragonal phase, the electron density is concentrated around the Pb and I atoms, indicative of their significant contribution to the electronic structure and the ionic nature of the bonding within the lattice. The electron density in the cubic phase, while still centered around Pb and I, shows a more dispersed nature, suggesting a different bonding environment possibly due to the polymorphous nature of the cubic structure. The electronic properties were studied by calculating the electronic band structures and the density of states (DOS). Fig. S5b and e show the band structure plots obtained from the PBE-GGA approximation. The k paths used for the calculations are X - M - Γ - R - X for the cubic and tetragonal phases. All the two structures of the compound were found to exhibit a direct band gap with a semiconductor characteristic. The cubic $MAPbI_3$ had the CB minimum and VB maximum located at the point Γ. The tetragonal $MAPbI_3$ had the CB minimum and VB maximum located at the point X. The calculated band gaps and crystal lattice parameters using the that approximations are given in Table S1. The band gap for the tetragonal phase is estimated at 1.63 eV, while the cubic phase is slightly lower at 1.57 eV.

The partial density of states (PDOS) plots of Fig. S5c and f reveal the contributions of different atomic orbitals to the electronic states. The sharp peaks in the valence band region, dominated by Pb and I p orbitals, suggest strong bonding interactions, while the conduction band is characterized by states that are more delocalized. The band gap, visualized in the DOS, confirms the direct nature of the transition, with a clear separation between the valence and conduction bands.

Table S1: Characterization of $MAPbI_3$ through DFT: lattice parameters and band gaps.

Parameter	Tetragonal	Cubic
Symmetry	I4/cm	Pm3m
a (Å)	8.8984	6.4759
b (Å)	8.8984	6.4759
c (Å)	13.2375	6.4759
$\alpha = \beta = \gamma$ (deg)	89.85	89.91
V (Å^3)	1050.13	271.58
Band gap (eV)	1.63	1.57

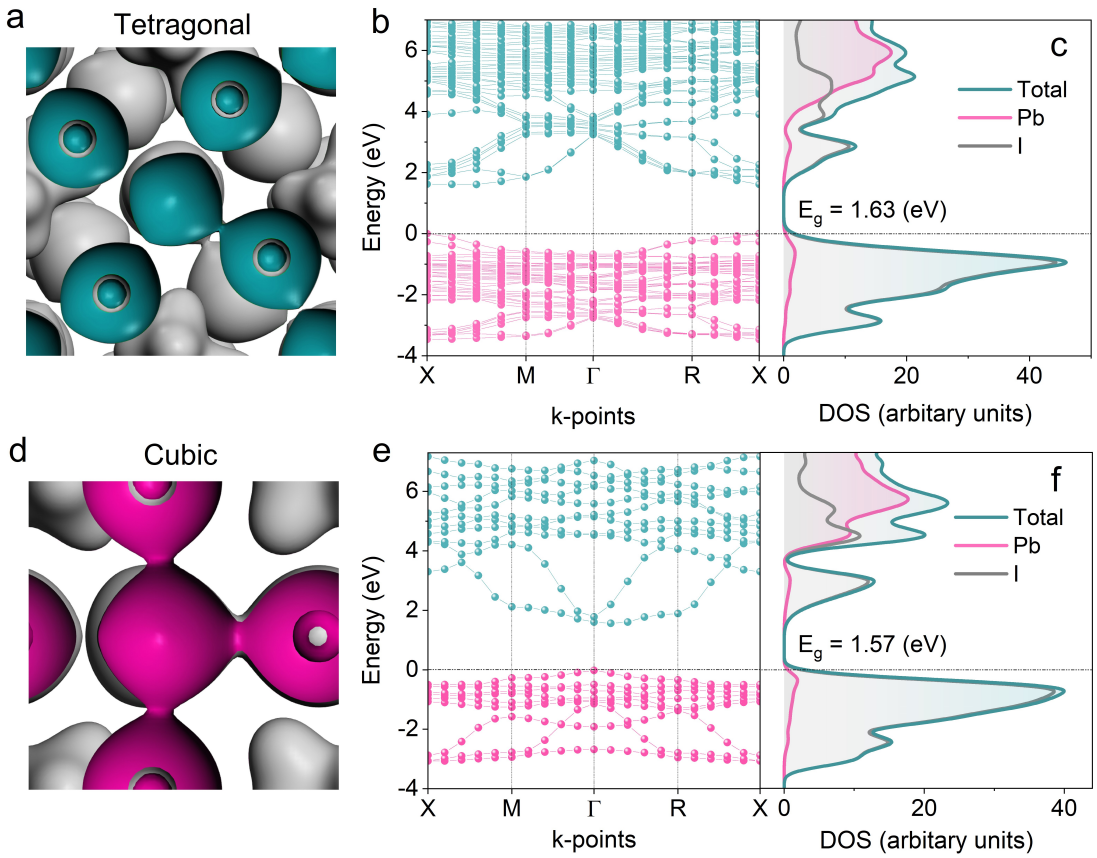

Fig. S5 DFT calculations: (a) & (d) electron density maps, (b) & (e) band structure, and (c) & (f) partial density of states of $MAPbI_3$ phases.

Supplementary Note S2:

We transformed 2D SEM images into 3D surface plots using ImageJ software [1]. We first calibrated the 2D images to a known scale for accuracy. Next, we used thresholding techniques to segment the nanoparticles from the background. A surface plotting algorithm then constructed the 3D topology. These 3D SEM images, as shown in Fig. S6 provide a detailed view of nanoparticle morphology, offering insights into nucleation and growth mechanisms not visible in 2D images.

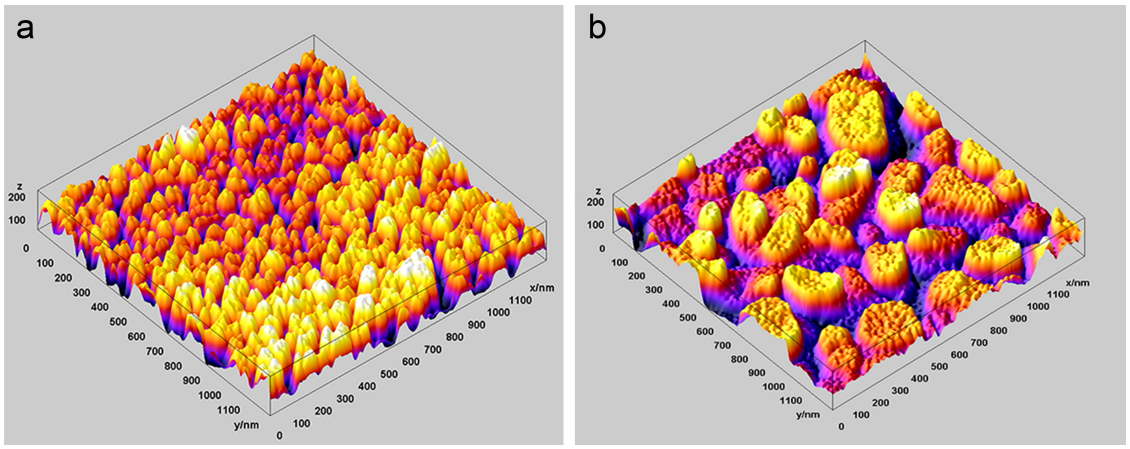

Fig. S6 3D scanning electron microscopy analysis of $MAPbI_3$: (a) AC and (b) DC. AC synthesis yields uniform nanoparticles, suggesting a controlled process, while DC treatment results in irregular particles, indicating stochastic influences.

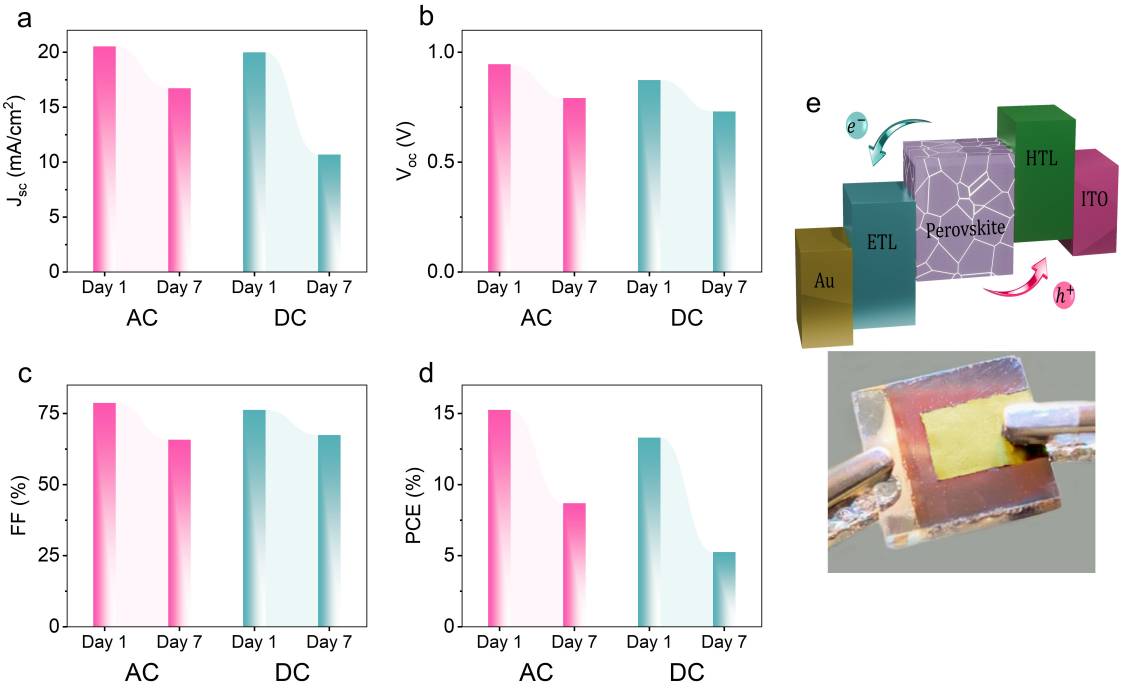

Fig. S7 Stability analysis of PSCs under AC and DC NTP. Panels (a) to (d) show the variation in key performance parameters over seven days: (a) short-circuit current (Jsc), (b) open-circuit voltage (Voc), (c) fill factor (FF), and (d) power conversion efficiency (PCE). Panel (e) illustrates the device architecture, and the photograph depicts the fabricated PSC. The results demonstrate that solar cells under AC conditions exhibit better stability and efficiency compared to those under DC conditions.

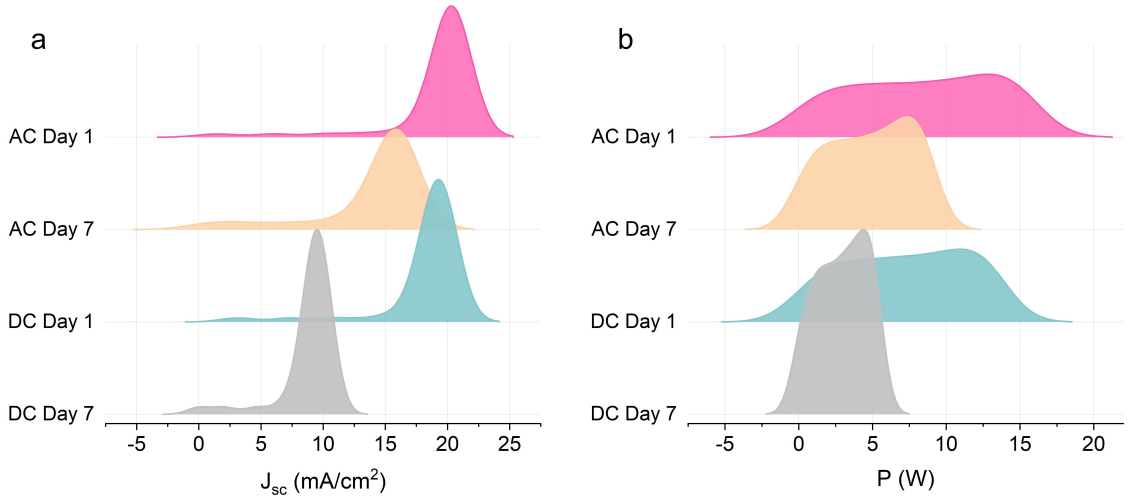

Fig. S8 Kernel distributions of (a) short-circuit current density and (b) power output for perovskite solar cells synthesized using AC and DC NTP over a period of seven days.

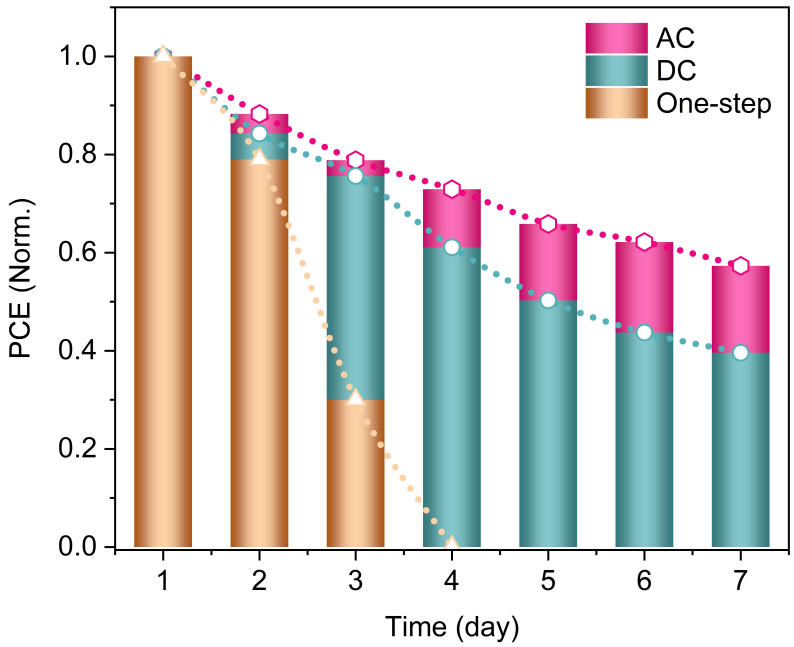

Fig. S9 Normalized PCE comparison for PSCs fabricated using AC, DC non-thermal plasma, as well as one-step method with annealing. Highlighting enhanced stability and retention for plasma-assisted techniques.

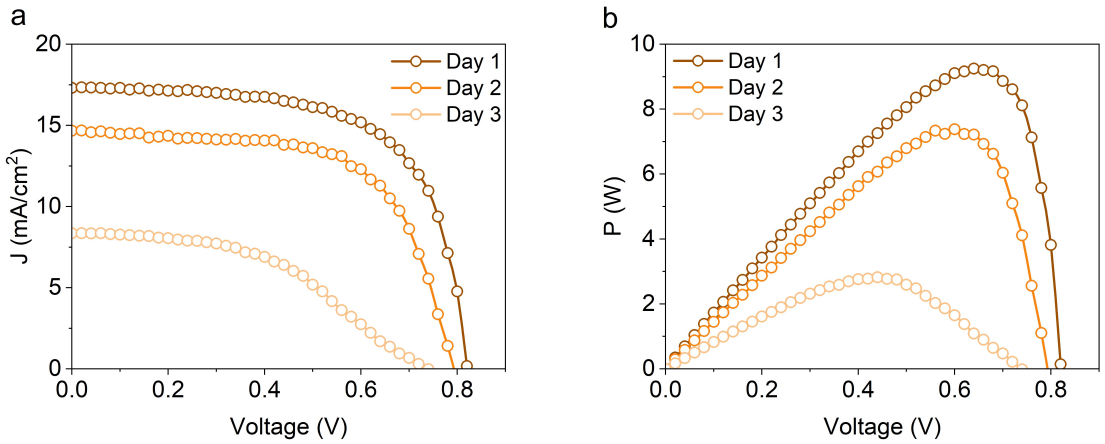

Fig. S10 Photovoltaic performance of perovskite solar cells over 3 days, showing a decline in current density (a) and power output (b) after synthesis via one-step method with annealed on a hot plate.

Table S2: Photovoltaic parameters of perovskite solar cells fabricated using a one-step method with a hot plate-assisted crystallization process.

	J_{SC} (mA/cm^2)	V_{OC} (V)	FF (%)	PCE (%)
Day 1	17.31	0.821	65.15	9.25
Day 2	14.67	0.792	63.55	7.38
Day 3	8.35	0.737	45.90	2.82

Supplementary Note S3:

Using the NTP synthesis technique, we modify the intrinsic properties of nanostructured perovskite materials. This approach improves surface and bulk defects, leading to advanced passivation and highlighting the importance of field-effect mechanisms see Fig. S11. Defects in the material create numerous recombination sites on the surface and within the bulk, reducing the device's efficiency [2]. We tackle this issue with a detailed passivation strategy that targets and reduces these recombination sites, improving device performance. Field-effect and surface passivation, utilizing AC-NTP rich in charged ions and electrons, to create an electrostatic barrier that repels charge carriers from defect sites. The essence of field-effect passivation lies in modifying the electric field at or near the perovskite interfaces. This modification helps separate photo-generated charge carriers, elevating the device's efficiency and stability.

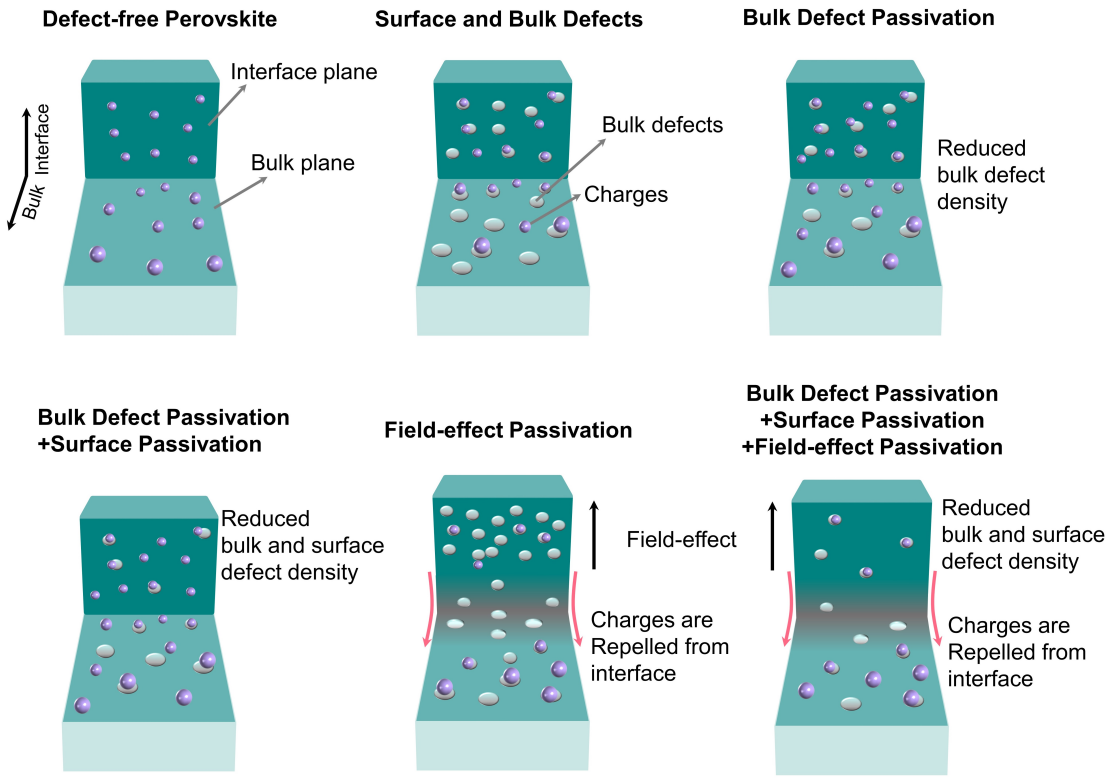

Fig. S11 Illustrations portray varied passivation techniques for perovskites, differentiating between bulk, interfaces and, field-effect passivation.

Materials and Methods

Chemicals

To synthesize perovskite nanoparticles and fabrication of PSCs, Methylamine (MA, 40 wt% in water), Hydroiodic acid (HI, 57 wt% in water), Lead Iodid (PbI_2, ≥99%), N, N−dimethyl formamide (DMF, ≥99.9%), Poly(3,4-ethylenedioxythiophene)-poly(styrenesulfonate) (PEDOT:PSS, ≥99.9%), and [6,6]-Phenyl-C71-butyric acid methyl ester (PCBM, ≥99.9%) obtained from Sigma-Aldrich (Merck).

Synthesis Procedure and Device Fabrication

The glass/ITO was cleaned by acetone and isopropyl alcohol using ultrasonic bath for 10 min and dried in the vacuum oven at 80 °C for 30 min. PEDOT:PSS was spin-coated on glass/ITO surface at 2000 rpm for 40 seconds and then annealed at 150 °C for 30 min in ambient air. The synthesis of $CH_3NH_3PbI_3$ perovskite is a precise process that begins with the organic precursor MAI. We first synthesize this precursor by reacting methylamine with hydroiodic acid, as described in Ref [3]. Then, we combine MAI and PbI_2 in a 1:1 molar ratio and add DMF as the solvent in a volume four times the mass of the precursors (specifically, we used 1 g of PbI_2, 0.64 g of DMF, and 0.34 g of CH_3NH_3I), see Fig. S12a. This mixture is homogenized using a dedicated stirring phase at ambient conditions for 10 minutes.

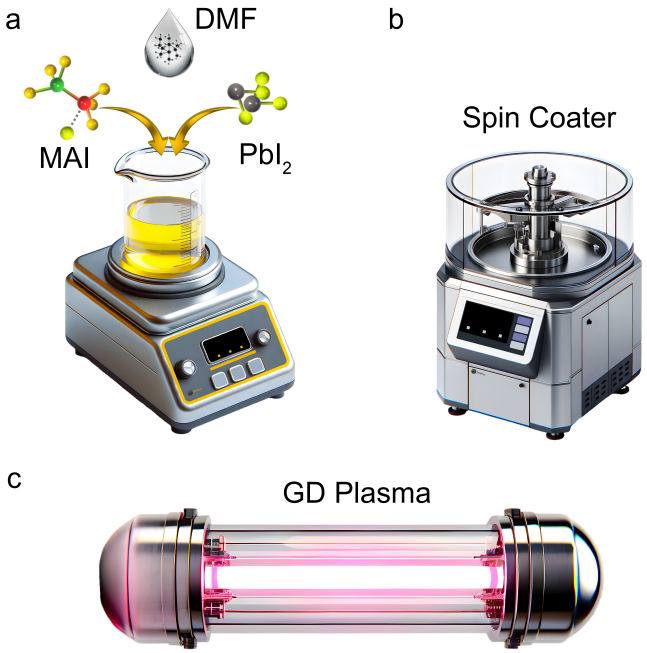

Fig. S12 Synthesis procedure of $CH_3NH_3PbI_3$ perovskite via non-thermal plasma method: (a) homogenization, (b) spin-coat deposition, and (c) glow discharge plasma consolidation.

The precision of the spin-coating step is evident from Fig. S12b, where the parameters are optimized to 2000 rpm for 10 seconds, to produce a thin, uniform film on the substrates. After that, the perovskite films were transferred into the NTP-assisted crystallization process, demonstrated in Fig. S12c, lasted 2 minutes in a nitrogen atmosphere with AC and DC NTP sources at a pressure of 0.2 mbar (for further details, see supplementary movie 1). This indicates a low-pressure NTP environment, which optimizes ion energy and density for crystallization. Subsequently, a solution of PCBM was spin-coated on the DC/AC treated perovskite layer/PEDOT:PSS/ITO/glass substrates at 2000 rpm for 40 seconds. Lastly, 100 nm of gold was thermally evaporated on top of PCBM surface.

The reference device was fabricated using the same steps as the main methods, except the perovskite layer was fabricated by one-step method with annealed on a hot plate at 120 °C for 12 minutes. All other layers and processing conditions were identical to ensure a fair comparison of PCE between the methods.

Characterization

The current-voltage characteristics were measured with a digital source meter (Keithley 2400) with the device under one-sun illumination (AM 1.5G, 100 mW cm^{-2}). The measurements were conducted with forward scan (FS) from -0.2 to 1.2 V or reverse scan (RS) from 1.2 to -0.2 V at a scan rate of 200 mV s^{-1}. X-ray diffraction (XRD) patterns were obtained using a X-ray diffractometer (Siemens XRD-D5000) with Cu K_α irradiation (λ = 1.5418 Å). Scanning electron micrographs (SEM) were acquired using a Tescan MIRA3 microscope to investigate the morphology of the materials and the grain size distribution was calculated using ImageJ software. To evaluate the optical properties of the synthesized perovskites, a Shimadzu UV-2450 spectrophotometer and a Jasco FP-6200 spectrofluorometer were utilized. Photoluminescence (PL) measurements were conducted on a glass substrate with an excitation wavelength of 220 nm.

PSCs Stability Analysis Method

Our method involves a systematic investigation of degradation factors in PSCs. Initially, we synthesize 14 identical sample structures, incorporating ITO, PEDOT:PSS, the perovskite active layer synthesized by AC and DC NTP, and PCBM, divided into two groups of seven for each treatment type. These samples are then subjected to constant illumination in ambient conditions (RH <40%) without encapsulation to simulate various degradation scenarios. Each day, one sample is selected, and we complete our device fabrication by adding PCBM and Au layers for a comprehensive J-V analysis. This daily evaluation allows us to assess the PSCs' stability over time thoroughly.

Reactor Characteristics

The plasma treatment procedure was carried out at room temperature using a non-thermal glow discharge plasma reactor. This reactor comprised a Pyrex tube with an internal diameter of 5 cm, sealed at both ends with aluminum bonnets, and had an overall length of 40 cm. Nitrogen was utilized as the plasma gas, and the plasma was generated using a high-voltage AC and DC generator operating at 1.5 kV and 20 Watts, with an AC frequency ranging from 12 to 18 kHz. Vacuum conditions were maintained using pumps capable of achieving 150 microns (0.15 mbar) and providing 1.4 horsepower.

Computational Method

Our theoretical calculations are based on the DFT as implemented in the Quantum Espresso (QE) simulation package [4] and VESTA [5] for supercell, nanocluster, and different phases built for $CH_3NH_3PbI_3$. The electronic structure of $MAPbI_3$ was carried out in two distingue crystal structures: tetragonal ($I4/cm$) and cubic ($Pm3m$). We used a supercell composed of $2 \times 2 \times 2$ repetition of the unit cell and let them relax. In nanocluster, we use spherical geometry with 20 nm diameter. For the relaxation in tetragonal, cubic, and nanocluster cells, we used the generalized gradient approximation (GGA) developed by Perdew-Burke-Ernzerhof (PBE) and implemented for solids PBESol [6–8]. We employ a plane wave cutoff of 400 eV for atomic relaxation, a $3 \times 3 \times 2$ k-point mesh for a tetragonal cell, and the same density for the cubic one. The electronic structure, including the density of states (DOS), was calculated using the GGA for the exchange-correlation function. GGA improves upon the local density approximation (LDA) by incorporating the electron density gradients, offering a more accurate description of the exchange and correlation effects, especially in systems with non-uniform electron distributions [9, 10]. This approach is particularly advantageous for simulating the electronic properties of materials, as it provides a balanced trade-off between computational efficiency and the accuracy of predicted electronic structures. It is important to note that our optical property calculations do not include exciton effects and are limited to the band edge region.

References

[1] Schindelin, J., et al. (2019). Fiji: an open-source platform for biological-image analysis. *Nat Methods*, *9*, 676–682. https://doi.org/10.1038/nmeth.2019

[2] Aydin, E., et al. (2019). Defect and Contact Passivation for Perovskite Solar Cells. *Advanced Materials*, *31*(25), 1900428. https://doi.org/10.1002/adma.201900428

[3] Peng, X., et al. (2016). Size-controlled synthesis of highly luminescent organometal halide perovskite quantum dots. *Journal of Alloys and Compounds*, *687*, 506-513. https://doi.org/10.1016/j.jallcom.2016.06.162

[4] Giannozzi, P., et al. (2009). QUANTUM ESPRESSO: a modular and open-source software project for quantum. *Journal of Physics: Condensed Matter*, *21*(39), 395502. https://doi.org/10.1088/0953-8984/21/39/395502

[5] Momma, K., et al. (2008). VESTA: a three-dimensional visualization system for electronic and structural analysis. *Journal of Applied Crystallography*, *41*(3), 653–658. https://doi.org/10.1107/S0021889808012016

[6] Perdew, J. P., et al. (1996). Generalized Gradient Approximation Made Simple. *Physical Review Letters*, *77*(18), 3865–3868. https://doi.org/10.1103/PhysRevLett.77.3865

[7] Monkhorst, H. J., et al. (1976). Special points for Brillouin-zone integrations. *Physical Review B*, *13*(12), 5188–5192. https://doi.org/10.1103/PhysRevB.13.5188

[8] Perdew, J. P., et al. (2008). Restoring the Density-Gradient Expansion for Exchange in Solids and Surfaces. *Physical Review Letters*, *100*(13), 136406. https://doi.org/10.1103/PhysRevLett.100.136406

[9] Borlido, P., et al. (2020). Exchange-correlation functionals for band gaps of solids: benchmark, reparametrization and machine learning. *npj Computational Materials*, *6*, 96. https://doi.org/10.1038/s41524-020-00360-0

[10] Dasgupta, S., et al. (2021). Elevating density functional theory to chemical accuracy for water simulations through a density-corrected many-body formalism. *Nature Communications*, *12*, 6359. https://doi.org/10.1038/s41467-021-26618-9